

ANELASTIC AND COMPRESSIBLE SIMULATIONS OF STELLAR OXYGEN BURNING

CASEY A. MEAKIN¹ & DAVID ARNETT¹

Draft version July 23, 2018

ABSTRACT

In this paper we compare fully compressible (Meakin & Arnett 2006a,b) and anelastic (Kuhlen, Woosley, & Glatzmaier 2003) simulations of stellar oxygen shell burning. It is found that the two models are in agreement in terms of the velocity scale ($v_c \sim 10^7$ cm/s) and thermodynamic fluctuation amplitudes (e.g., $\rho'/\langle\rho\rangle \sim 2 \times 10^{-3}$) *in the convective flow*. Large fluctuations ($\sim 11\%$) arise in the compressible model, localized to the convective boundaries, and are due to internal waves excited in stable layers. Fluctuations on the several percent level are also present in the compressible model due to composition inhomogeneities from ongoing entrainment events at the convective boundaries. Comparable fluctuations (with amplitudes greater than $\sim 1\%$) are absent in the anelastic simulation because they are due to physics not included in that model. We derive an analytic estimate for the expected density fluctuation amplitudes at convective boundaries by assuming that the pressure fluctuations due to internal waves at the boundary, p'_w , balance the ram pressure of the convective motions, ρv_c^2 . The predicted amplitudes agree well with the simulation data. The good agreement between the anelastic and the compressible solution within the convection zone and the agreement between the stable layer dynamics and analytic solutions to the non-radial wave equation indicate that the compressible hydrodynamic techniques used are robust for the simulated stellar convection model, even at the low Mach numbers found $M \sim 0.01$.

Subject headings: stars: evolution - stars: nucleosynthesis - massive stars - hydrodynamics - convection - g-modes

1. INTRODUCTION

Oxygen burning (by $^{16}\text{O} + ^{16}\text{O}$ fusion) occurs in the precollapse stages of the evolution of massive stars. Neutrino cooling speeds these stages to the extent that the evolutionary times scales are close enough to the sound travel time so that direct compressible numerical hydrodynamics can be applied (Arnett 1994). The first detailed studies of this stage (Bazán & Arnett 1998) were done in two-dimensional symmetry (2D) with PROMETHEUS (Fryxell, Müller, & Arnett 1989), a multi-fluid multidimensional compressible hydrodynamics code based on the Piecewise Parabolic Method (PPM) of Colella & Woodward (1984). They showed vigorous convection, with significant density fluctuations (up to 8%) at the convective-nonconvective boundaries. These results were confirmed in detail in 2D with the VULCAN Arbitrary-Lagrangian-Eulerian (ALE) hydrodynamics code (Livne 1993) by Asida & Arnett (2000). VULCAN is an entirely independent compressible hydrodynamics code, so that these two sets of simulations only shared the initial model, the sonic time step limitation, and the 2D geometry. A new version of the PROMETHEUS code, PROMPI (which uses the Message Passing Interface for parallelism), has extended the study to 3D. In all these compressible models except the earliest (Arnett 1994) the computational domain has included both the convective oxygen burning shell as well as two bounding stably stratified layers.

Kuhlen, Woosley, & Glatzmaier (2003) investigated shell oxygen burning in 3D using an anelastic hydrodynamics code which filters out sound waves and linearizes

thermodynamic fluctuations around a background reference state (Glatzmaier 1984; Gough 1969). In contrast to the fully compressible results above, Kuhlen, Woosley, & Glatzmaier (2003) found only small density and pressure contrasts, and subsonic flows which were well within the anelastic approximation (all thermodynamic contrasts less than 1 percent). The boundary conditions used were impermeable and stress-free and were placed within the convection zone so that convective overshoot could not be studied. In particular, the dynamic consequences of the neighboring non-convective shells, and their elastic response to convective fluctuations, were ignored. The formulation was single fluid, so that effects depending upon composition, i.e., mixtures of fuel and ashes, were not modeled.

The applicability of both fully compressible and anelastic hydrodynamic methods have recently been challenged by developers of low-Mach number solvers (Almgren et al. 2006). The reliability of compressible codes has been questioned for low velocity flows due to possible violations of elliptic constraints that arise in the evolution equations in the very small Mach number limit (e.g., Schneider et al. 1999). The limits for which compressible solvers remain robust in the astrophysical context, however, has not been rigorously studied. Anelastic methods, on the other hand, enforce a divergence constraint on the velocity field which filters out sound waves, but are formulated assuming that thermodynamic fluctuations are small and only linear deviations from a background reference state are retained. Therefore, this approximation is expected to fail for models which include large gradients in the thermodynamic variables such as occur at the boundaries of shell burning regions.

The correct identification of the behavior in shell oxygen burning has wide implications. This stage of massive

Electronic address: cmeakin@as.arizona.edu, darnett@as.arizona.edu
¹ Steward Observatory, University of Arizona, 933 N. Cherry Avenue, Tucson, AZ 85721

star evolution is important for a variety of topics of current research interest (e.g., Young, et al. (2005, 2006)). In this paper we discuss the quantitative similarities and differences between the models of oxygen shell burning which we have introduced above and show that the two models are in good agreement with each other. In addition, the compressible models are in agreement with scaling relations derived from the basic hydrodynamic equations as well as analytic solutions to the non-radial wave equation for motions in the stable layers. These findings lend strong support to the validity of both simulations. There are no signs that either the anelastic or the PPM method is breaking down for the conditions simulated, even in regions of the flow where the Mach number does not exceed $M \sim 0.01$.

2. MODEL COMPARISON

2.1. The Initial Models and Simulation Parameters

In Table 1 we summarize the initial conditions, computational domains, zoning, and properties of the developed flow for the three models that we will discuss in this paper. These include a 2D and a 3D compressible model calculated with the PPM method (Meakin & Arnett 2006a,b) and the non-rotating anelastic model described by Kuhlen, Woosley, & Glatzmaier (2003). The initial conditions for the compressible simulations are of a $23 M_{\odot}$ star previously evolved with the TYCHO stellar evolution code (Young & Arnett 2005) which is directly mapped onto the hydrodynamics grid. A 25 nuclei reaction network is used to track composition and energy generation. The computational domain for the compressible models are restricted to fractions of a sphere and use a spherical coordinate system. The 2D model is a 90° wedge embedded in the equatorial plane, and the 3D model is a wedge of $30^{\circ} \times 30^{\circ}$ degrees centered on the equator. The radial limits for these models enclose both the convectively unstable oxygen burning shell, as well as two surrounding stably stratified layers. Boundary conditions, which are *placed in the stable layers*, are impermeable and stress free. The net energy generation due to nuclear burning and neutrino cooling, $L_{net} = \int (\epsilon_{nuc} + \epsilon_{\nu}) dM \approx 3.5 \times 10^{46}$ erg/s, is positive and goes into PdV work through a background expansion which develops naturally in the compressible model in the same way it does in the initial TYCHO model.

The anelastic model uses a reference state which is a polytropic fit to a $25 M_{\odot}$ stellar model which was evolved with the KEPLER code (Weaver et al. 1978). A multi-fluid model and reaction network are not used and nuclear energy generation is instead estimated using a power law fit for density and temperature dependence. The anelastic model uses spherical harmonics for angular coverage, ameliorating the pole singularity problem of a spherical coordinate system, and covers a full 4π steradians. Chebyshev polynomials are used in the radial direction. The radial limits of the anelastic model enclose *only the convection zone with no regions of stable stratification*. The boundary conditions, which are within the unstable convective layer, are also impermeable and stress free. The net energy generation is positive, $L_{net} \approx 1.5 \times 10^{45}$ erg/s. The anelastic model used is unable to model background expansion so the excess energy is forced to escape from the outer boundary of the calculation. The lower net energy generation of this

model may be due to it being in a later evolutionary stage.

Both hydrodynamic models use the equation of state provided by Timmes & Swesty (2000). The radial limits of the oxygen burning convection zone and enclosed mass for the two initial models evolved with the KEPLER and TYCHO codes are remarkably similar. The compressible model uses 400 logarithmically spaced radial zones (to keep zone aspect ratio $dr/r d\theta \sim 1$) and an angular resolution of $\sim 0.3^{\circ}$ per zone. The anelastic model uses 145 zones for a comparable radial extent, and spherical harmonics up to order $l = 63$ to cover the sphere which is roughly equivalent to a Nyquist sampling of $\sim 1.5^{\circ}$ per zone, approximately a factor of five lower angular resolution than the compressible model. The Rayleigh and Reynolds numbers quoted by Kuhlen, Woosley, & Glatzmaier (2003) are $Ra \sim 5 \times 10^7$ and $Re \sim 3000$. Since the compressible model is more strongly driven (larger L_{net}) and has finer zoning (resulting in a lower effective viscosity), both the effective Rayleigh and Reynolds numbers will be higher in the compressible model.

2.2. Flow Properties: Anelastic Model

The anelastic simulation has been run for 6500 seconds. With an average flow velocity of $v_c \approx 0.49 \times 10^7$ cm/s, and a radial extent for the convection zone $\Delta R \approx 0.39 \times 10^9$ cm the turnover time $t_c = 2\Delta R/v_c \approx 159$ seconds and the simulation spans approximately 41 convective turnovers. The peak velocity is given as $v_{peak} \approx 1.8 \times 10^7$ cm/s which corresponds to a peak Mach number $M \sim 0.04$ for a sound speed $c_s \approx 4.5 \times 10^8$ cm/s. The maximum density fluctuations within the convection zone are found to be of the order $\rho'/\langle\rho\rangle \sim 2 \times 10^{-3}$ which is the same order of magnitude as the peak Mach number squared, $M^2 \sim 1.6 \times 10^{-3}$ consistent with the scaling arguments for the anelastic approximation for thermal convection (Gough 1969).

2.3. Flow Properties: Compressible Models

The flow in the compressible simulations consists of two distinct regimes: the turbulent convection zone, and the wave-bearing stably-stratified layers. These can be quite readily discerned in the density fluctuation field shown in Figure 1. In this section we discuss these two regimes in turn for the three dimensional model, and then discuss the properties of the two dimensional model.

The three dimensional compressible model was run for ~ 800 seconds of star time. The average flow velocity is found to be $v_c \approx 0.8 \times 10^7$ cm/s. With a convection zone width $\Delta R \approx 0.41 \times 10^9$ cm the turnover time is $t_c \approx 103$ seconds and the simulation spans approximately 8 convective turnovers. After an adjustment in the initial size of the convection zone due to penetrative convection (Meakin & Arnett 2006a,b), the flow achieves a steady state within ~ 200 seconds, or two convective turnovers, after which the average flow properties do not change appreciably. Figure 2 shows the peak density fluctuation and the Mach number at each radius for the three dimensional model. Within the convection zone, $0.44 \lesssim r/10^9 \text{ cm} \lesssim 0.85$, the maximum density fluctuation and Mach number are $\rho'/\langle\rho\rangle \sim 5 \times 10^{-3}$ and $M \sim 0.09$, respectively. Here also, the fluctuation scale is the same order of magnitude as the peak Mach number squared,

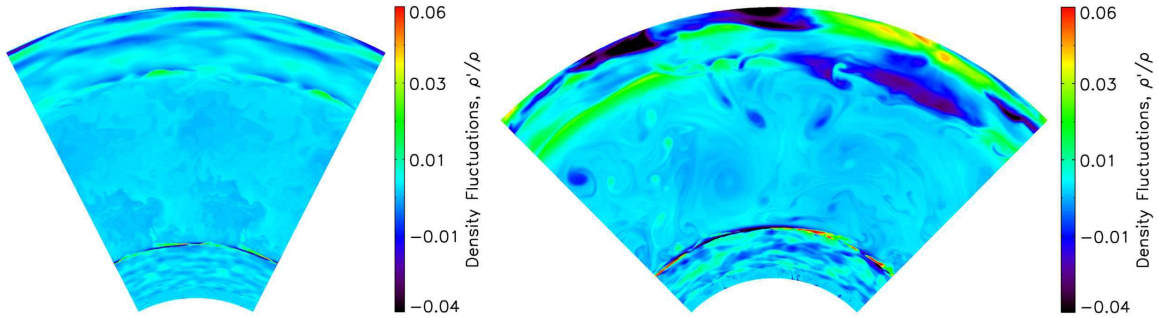


FIG. 1.— Spatial distribution of density fluctuations are shown for (left) a slice through the 3D compressible model and (right) the 2D compressible model. In both models the flow is composed of two distinct regimes, including the convective flow in the center which is bounded above and below by stably stratified layers which are host to internal waves. The scale on the 2D model has been truncated to same limits as the 3D model for comparison, but extreme values exceed the scale limits by a factor of ~ 2 . The 3D model has been tiled twice in angle for clarity.

$M^2 \sim 8 \times 10^{-3}$. The rms Mach number in the convection zone is $M_{rms} \sim 0.01$.

These velocity and fluctuation scales are comparable to those of the 3D anelastic model and are listed in Table 1 for both simulations for comparison. The point we want to emphasize here is that *the character of the convective flow is quantitatively in agreement between the anelastic and compressible models*. We also find, from a detailed comparison to be presented separately (Meakin & Arnett 2006b), that the 3D compressible model compares well with the stellar mixing length theory (Kippenhahn & Weigert 1990), including the velocity scale ($v_c \sim 10^7$ cm/s) and the superadiabatic stratification ($\Delta \nabla \sim 5 \times 10^{-4}$). The slightly larger velocity scale in the compressible model can be attributed to the higher Rayleigh number due to the larger luminosity needed to be transported by the convective flow.

2.3.1. Additional Sources of Fluctuations

In this section we discuss the origins of thermodynamic fluctuations which are due to physics not included in the anelastic model of Kuhlen, Woosley, & Glatzmaier (2003), including stably stratified layers and composition effects. We begin with a discussion of the internal wave dynamics occurring near the convective boundaries.

Significant density fluctuations occur at the convective boundaries in the compressible model, reaching values as large as 11×10^{-2} , over twenty times larger than in the body of the convection zone (Figure 2 and Table 1). Examining the spatial distribution of the density fluctuations presented in Figure 1 reveals that the largest fluctuations occur at the interface between the convection zone and the stably-stratified, wave-bearing layers. The morphology of the largest density fluctuations in the domain (i.e., those at the convective boundary) are periodic in angle and harmonic in time, identifying them with internal wave dynamics. In the following discussion we present analytic estimates for the amplitudes of the density fluctuations at the convective boundary and show that they are in good agreement with the simulation data.

For small amplitude waves the Eulerian density fluctuations and pressure fluctuations are related by (Unno et al. 1989, p.93):

$$\frac{\rho'}{\langle \rho \rangle} = \frac{p'}{\langle p \rangle \gamma_{ad}} + \xi_r \frac{N^2}{g} + (\text{nonadiabatic terms}) \quad (1)$$

with buoyancy frequency N , and Lagrangian displacement ξ_r . We defer a discussion of nonadiabatic and composition effects to the end of this section. In the convection zone, material is nearly neutrally stratified and the buoyancy frequency is very close to zero so the second term on the right hand side is not very important. At convective boundaries the stellar structure assumes a stable stratification with a positive buoyancy frequency, and this term can become dominant. This term represents the component of the Eulerian density fluctuation due to g-mode oscillations and is the projection of the Lagrangian displacements of the wave, ξ_r , onto spherical shells. In the presence of steep density gradients, waves can lead to large Eulerian fluctuations even when compressibility is not important. To be as clear as possible on this key point, we give an analogy to well known physics: consider waves on a lake. The Lagrangian surface is the surface of the water. The Eulerian surface is the average level of the water and Eulerian density fluctuations occur as the waves (water) and troughs (air) move by the observer. The large variation in density is not due to compression, but the choice of coordinates (Eulerian in this case).

In order to estimate the amplitude of the density fluctuations using equation 1 we need to know the size of the pressure fluctuation and the maximum radial displacement amplitude, ξ_r^{\max} , for wave motions at the boundary. Both quantities can be estimated by assuming that the ram pressure of the convective turbulence is balanced by wave induced pressure fluctuations at the convective/stable layer interface:

$$\rho v_c^2 \approx p'_w. \quad (2)$$

The validity of this approximation is demonstrated in Figure 3, which shows that the RMS horizontal pressure fluctuations and the turbulent ram pressure are comparable in the convection zone and do indeed balance at the locations of the convective boundaries.

The relationship between the pressure fluctuation of an internal wave, p'_w , and the maximum radial displacement, ξ_r^{\max} , depends on the wave frequency σ and horizontal wavenumber k_h . Perhaps the simplest approximation is to assume that internal waves generated at the convective boundary are directly related to the convection through the convective velocity v_c and eddy scale, $l_c \sim H_p$, by $v_c \sim \sigma/k_h$ and $k_h \sim 2\pi/l_c$ in the spirit of stellar mixing length theory (Press 1981). Adopting

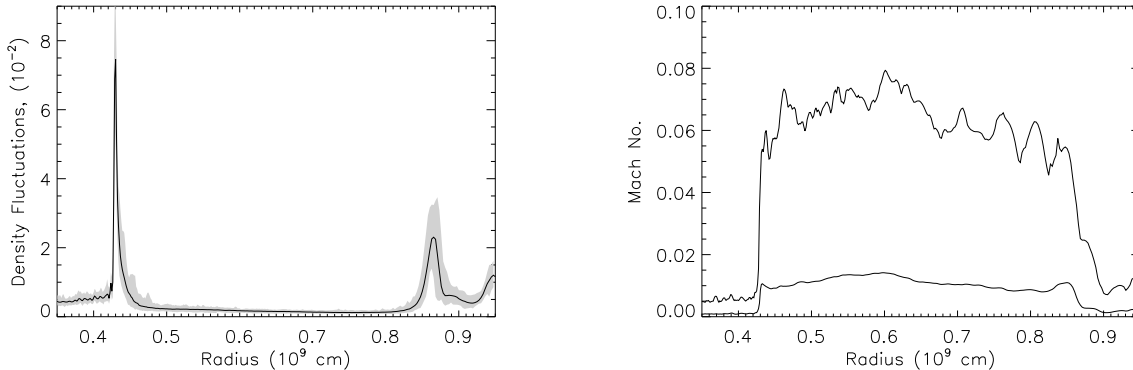


FIG. 2.— (left) Density fluctuations for 3D compressible model: The time average of the maximum density fluctuation is shown as the thick line, with the extreme values for the averaging period (two convective turnovers) shown as the shaded region. Within the body of the convection zone the average fluctuations are quite low $\sim 0.25\%$. The largest fluctuation (the spike at $r \approx 0.43 \times 10^9$ cm) is $\sim 11\%$ (exceeding the plot limits), while the secondary maximum ($r \approx 0.85 \times 10^9$ cm) reaches $\sim 3.5\%$. These fluctuations occur in the radiative regions that enclose the convection zone (outside the computational domain of Kuhlen, Woosley, & Glatzmaier (2003)). (right) Mach number for the 3D compressible model: shown is the instantaneous value of the maximum Mach number at a given radius (thick line), and the rms Mach number (thin line).

these values we can then use the linearized momentum equation (Unno et al. 1989, p.96),

$$\xi_h^{\max} \sim \frac{[l(l+1)]^{1/2} p'_w}{r\sigma^2} \approx \frac{k_h v_c^2}{\sigma^2} \quad (3)$$

and the dispersion relation (for waves in which $\sigma \ll N < L_l$),

$$k_h/k_r \sim \frac{\sigma}{N} \quad (4)$$

to estimate the radial displacement:

$$\xi_r^{\max} = \xi_h^{\max} \times k_h/k_r \sim \frac{k_h v_c^2}{\sigma^2} \frac{\sigma}{N} \sim v_c/N. \quad (5)$$

The dispersion relation used to connect the horizontal and radial displacement amplitudes is valid when the wave frequency is much smaller than both the buoyancy frequency and the Lamb frequency $L_l = k_h c_s$, with sound speed c_s , and is a reasonable approximation for the wave properties adopted above (where $\sigma/L_l \approx M_c$).

Here, our main result is the last expression in equation 5 for the radial displacement amplitude of the interfacial wave which is in pressure balance with the ram pressure of the convection. This expression is equivalent to the statement that the kinetic energy of the turbulent motion exciting the wave is balanced by the potential energy of the wave, which follows naturally from the basic energetic properties of waves in fluids (Lighthill 1978).

Finally, we use the displacement given by equation 5 and the pressure fluctuation in equation 2 with equation 1 to arrive at our estimate for the interfacial density fluctuation amplitude,

$$\frac{\rho'}{\langle \rho \rangle} \sim M_c^2 + \frac{v_c N}{g} \quad (6)$$

in terms of the Mach number M_c , gravity g , and buoyancy frequency N . Adopting flow parameters from the simulation ($v_c \sim 10^7$, $g \sim 10^9$ in cgs units) we find $\rho'/\langle \rho \rangle \sim (10^{-3} + N \times 10^{-2})$ with N in rad/s. The validity of this expression is apparent when comparing the

buoyancy frequency in Figure 3 with the density fluctuations at the convective boundaries in Figure 2.

It can also be seen that the density fluctuations throughout the stable regions, not just at the convective boundaries, are in rough agreement with the scaling given by equation 6, though the amplitudes in the stable layers drop off with distance from the convective boundary. This is due to a spectrum of internal wave modes excited at the convective boundaries, rather than the single mode assumed in the above analysis. Each modal component contributes to the pressure balance at the convective boundary and is composed of wave packets that travel back and forth within the resonating cavity of the stable layer (Unno et al. 1989) causing fluctuations throughout the region. A more detailed analysis is possible in which the entire spectrum of internal waves is estimated by matching the wave motions to those of the spectrum of turbulent convection (e.g. Carruthers & Hunt 1986). Our single mode approach, however, works very well in describing the amplitudes of the fluctuations at the convective boundaries and provides a reasonable upper limit to the fluctuations throughout the entire stable layer.

We conclude this section with a discussion of the role that entropy fluctuations play in setting the scale of density fluctuations and hence buoyancy of material in the convection zone. The non-adiabatic term in equation 1 takes the form,

$$\frac{\rho'}{\langle \rho \rangle} = \frac{v_T}{c_p} \delta S \quad (7)$$

with thermodynamic derivative $v_T = -(\partial \ln \rho / \partial \ln T)_p$, specific heat at constant pressure c_p , and Lagrangian entropy fluctuation δS . In the present model the largest non-adiabaticity is due to net effect of nuclear burning and neutrino cooling. The entropy fluctuation can then be written $\delta S_{nuc} = \delta Q_{net}/T \approx \epsilon_{net} \delta t/T$ where the time material dwells in the burning region is $\delta t \approx \Delta r/v_c \sim l_c/v_c \sim 10s$. For the nuclear energy release in the current model, with a peak burning rate of $\epsilon_{net} \sim 10^{14}$ erg/g/s, the maximum entropy fluctuation will be of order $\delta S_{nuc}^{\max} \sim 0.01$ in units of $N_A k_B$. The correspond-

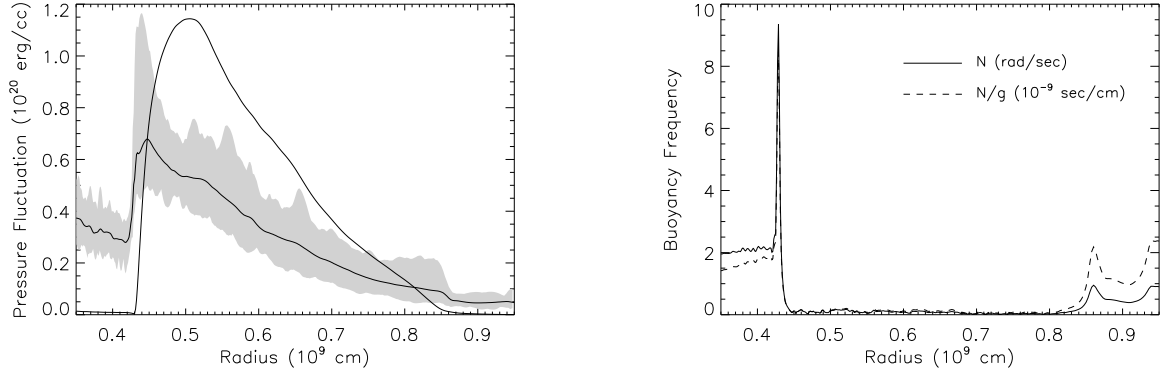


FIG. 3.— (left) Pressure fluctuations in 3D compressible model: The time averaged horizontal RMS pressure fluctuations are shown as the thick line, with the envelope of extreme values over two convective turnovers indicated by the shaded region. The radial ram pressure of the turbulent convection, ρv_r^2 , is shown as the thin line. The curves cross at the convective boundaries where the turbulent pressure is balance by the pressure fluctuation induced by internal waves in the adjoining stably stratified layers. (right) The buoyancy frequency in units of rad/s. Also shown as the dashed line is the buoyancy frequency normalized by the gravity which, through Equation 6, sets the scale of the density fluctuations at the convective boundaries (compare with Figure 2a).

ing maximum density fluctuation will be approximately $\rho'/\langle\rho\rangle|_{nuc} \sim 2.5 \times 10^{-3}$, which is of order the amplitude of the fluctuations due to the weak compressibility effects in the convective flow. These values compare well to the perturbations estimated using mixing length theory, consistent with the convective flow being driven by the nuclear burning luminosity in the shell.

Entropy fluctuations also occur within the convection zone due to composition inhomogeneities. The radial entropy profile and the RMS entropy fluctuations are presented in Figure 4. The fluctuations are due to: (1) interfacial wave motions which cause Eulerian fluctuations in the same manner as for the density fluctuations discussed above; and (2) the entrainment of high and low entropy material at the convective boundaries which is mixed into the nearly adiabatic convection zone. The wave induced fluctuations appear as spikes near the convective boundaries and are present in both the curve of minimum and maximum fluctuation. The regions affected by compositional inhomogeneities are labeled in Figure 4, with low entropy material entrained from below and high entropy material entrained from above. The entropy fluctuations associated with this material is another source of density fluctuations and explains the larger values that occur just within the boundaries of the convection zone in Figure 2. The entropy fluctuations associated with the entrained material are much larger than due to nuclear burning (the entropy perturbation in the region of greatest nuclear energy deposition, $r \sim 0.45 \times 10^9$ cm, is primarily *negative*). The entrainment of material from stable layers by a turbulent convective flow is an essential addition to stellar evolution modeling with significant consequences for the evolution of burning shells in presupernova models.

2.3.2. Dimensionality

It has long been known that 2D simulations were informative only to the extent that care is used in their interpretation. In 2D the vorticity is restricted to the direction normal to the computational domain, while in 3D instabilities cause its orientation to wander. Thus 2D is useful in situations in which there are physical reasons to enforce the symmetry (e.g., terrestrial cyclonic storms), but has nevertheless been used widely in more

general applications because of computer resource limitations. The increasing availability of computing clusters and software parallelization tools is now making 3D hydrodynamic simulation more common, and we are starting to assess the adequacy and limitations of earlier 2D work.

We have calculated a 2D compressible model for 2400 seconds of star time. We find an average flow velocity of $v_c \approx 2.0 \times 10^7$ cm/s and a convective turnover time of $t_c \approx 40$ seconds, so our simulation spans approximately 60 turnover times. The peak velocity during the course of the simulation is $\sim 5.5 \times 10^7$ cm/s, corresponding to a peak Mach number of $M \sim 0.163$. The density fluctuations within the convection zone reach a maximum value of $\rho'_c/\langle\rho\rangle \sim 6 \times 10^{-2}$. At the convective boundaries the density fluctuations attain a peak value of $\rho'_b/\langle\rho\rangle \sim 12 \times 10^{-2}$.

We find two significant differences between the 2D and 3D models. First, we find a significantly decreased turbulent mixing rate in the 2D simulation. Material entrained into the convection zone at the boundaries is pulled into the large cyclonic flow patterns in the 2D simulation where large composition inhomogeneities persists for several convective turnovers. In contrast, material entrained into the convection zone in the 3D models is homogenized within a single convective turnover time. This effect is illustrated in Figure 5, which shows the spatial distribution of oxygen abundance, as well as RMS fluctuations for both the 2D and 3D simulations. The 2D simulation retains high level fluctuations throughout the convective zone, while inhomogeneities in the 3D model are mixed to low levels by the time material completes a single crossing. Comparing Figures 5 and 1, which are snapshots at the same time, show the high entropy oxygen entrained at the top boundary corresponds to a negative density perturbation.

The second major discrepancy between the 2D and 3D models is the convective velocity scale. We find that both the mass averaged convective velocity and the peak velocity fluctuation are ~ 2 time larger in the 2D model. This velocity scale difference may be connected to the lower turbulent mixing efficiency in the 2D flow. We find that the net enthalpy flux, which consists of upward

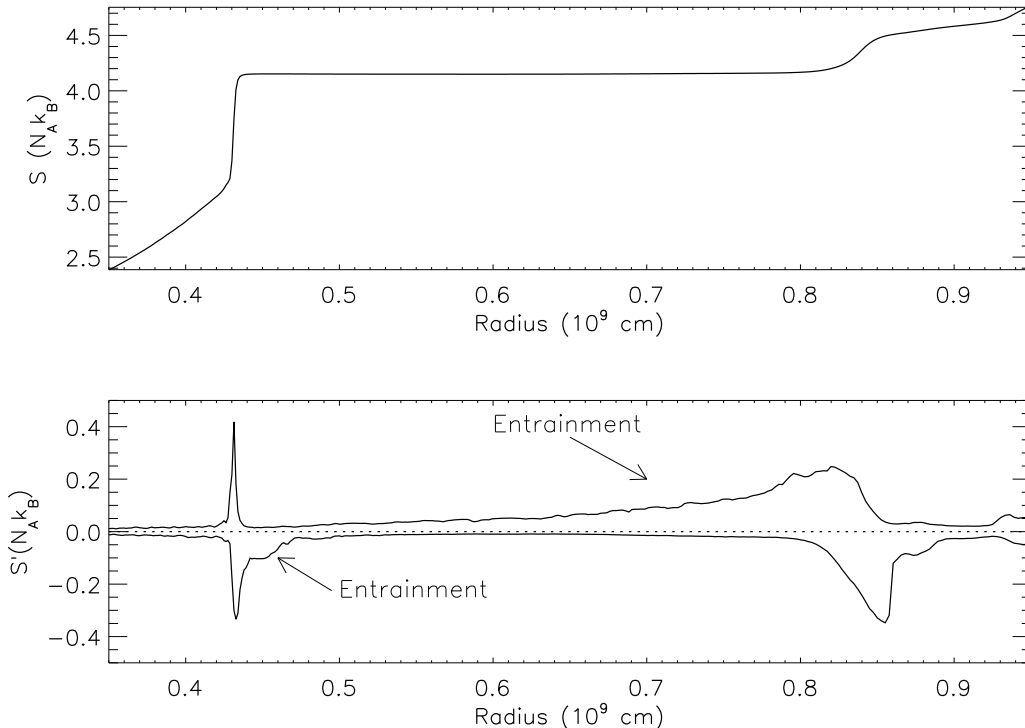


FIG. 4.— (top) Entropy profile of for 3D compressible model. (bottom) Entropy fluctuations for 3D compressible model: The two solid lines indicate the maximum and minimum fluctuation for a given radius over the course of two convective turnovers. The annotations indicate fluctuations due to low entropy material entrained at the lower boundary and high entropy material entrained at the upper boundary.

and downward directed components, $F_{net} = F_{up} - F_{down}$, is the same between the 2D and 3D models. In the 2D model, however, the relative value of the individual flux components relative to the net flux, e.g., F_{up}/F_{net} , are much larger than in the 3D model. Therefore, the 2D model requires a larger velocity scale to move the same net flux due to the inefficiency of depositing the advected enthalpy across the convection zone.

We find that 2D and 3D models compare well in the wave region, but differ in the convection zone. The 3D convection is more similar to that of the anelastic model of Kuhlen, Woosley, & Glatzmaier (2003) and the values predicted by mixing length theory. While waves behave similarly in 2D and 3D, turbulent convection does not, particularly with regards to turbulent mixing efficiency. Although the spatial resolution of the 2D and 3D models are the same, the number of degrees of freedom in the angular direction is much larger in the 3D model, $N_{3D}/N_{2D} = (100)^2/320 \sim 31$. If the number of degrees of freedom were the only important parameter, one might wonder if 2D would provide a more efficient surrogate to 3D. It turns out that 2D is actually more expensive than 3D because the same degrees of freedom in 2D requires a higher spatial resolution and hence a more severe time step constraint, and computational cost is $N_{cost} \propto N_{space} \times N_{time}$.

3. CONCLUSIONS

A comparison between the flow properties in fully compressible and anelastic simulations of stellar oxygen shell burning indicate that the two methods produce quantitatively similar results. Both methods produce convective

flows in 3D models which are compatible with the results expected for the mixing length theory of convection for this phase. The compressible models have been extended to include additional physics not included in the anelastic model, namely stably stratified boundary layers and a multi-fluid flow ($N_{species} = 25$). The interaction between the convection and the stable layers excite internal waves which produce larger thermodynamic fluctuations (up to 11% in 3D). Composition inhomogeneities due to ongoing entrainment events at the convective boundaries also cause density fluctuations on the several percent level, though material is homogenized rapidly in the 3D model through turbulent mixing.

The relatively large fluctuation which arise at the convective boundaries $\sim 11\%$ may stress the reliability of the anelastic approximation if this region is to be included in future simulations of oxygen burning or later epochs, where entropy and density gradients are large. A variety of convection studies have shown that boundary condition type (e.g., hard wall compared to stable layer) alters the overall flow pattern within a convection zone (Hosain & Mullan 1993; Rogers & Glatzmaier 2005b) and therefore the astrophysically correct conditions should be used. Low Mach number solvers (e.g. Lin et al. 2006) may be the most efficient tools for extending studies of oxygen and silicon shell burning to full spherical domains in 3D while retaining the crucial density gradients at the convective boundaries where convective penetration and entrainment operate, and asymmetric fluctuations arise which may have important implications for the evolution of pre-supernova models. Earlier stages such as carbon and neon burning have both milder flows and shallower

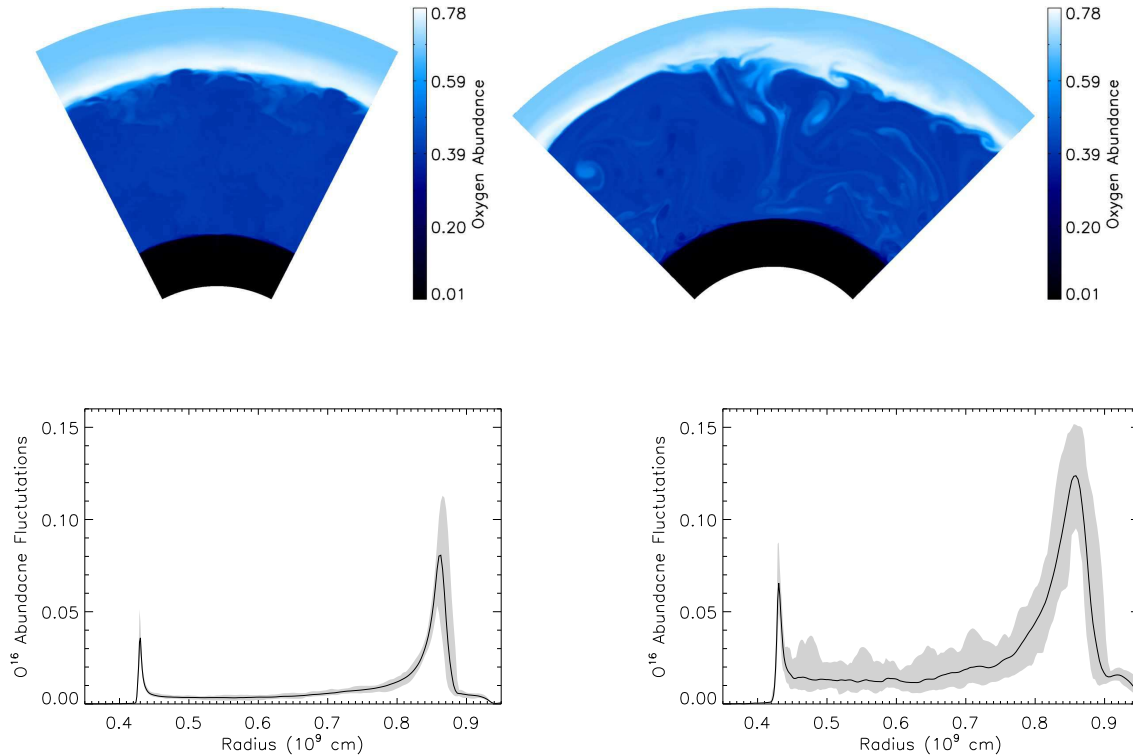


FIG. 5.— Spatial distribution of the oxygen mass fraction is shown for (left panels) the 3D compressible model and (right panels) the 2D compressible model. The spatial distribution is shown in the top row, and the time averaged RMS horizontal fluctuations are shown in the bottom row with the shaded region indicating extreme values of the fluctuations over two convective turnovers.

density gradients and should be better suited for anelastic methods, even at convective boundaries. Background expansion and multi-fluid effects should be included however. The large time step advantage of the anelastic and low Mach number simulations allows for much larger domains or better resolution.

Although the efficiency of fully compressible hydrodynamics may be low for the Mach numbers modeled, there are no signs that the solver used is breaking down in the oxygen shell burning simulations presented here. This conclusion is supported on several grounds, including: (1) The compressible model is in good agreement quantitatively with the anelastic methods for the convection zone region, including the velocity scales, and thermodynamic fluctuation amplitudes, a region in which the anelastic method is expected to perform well. (2) The compressible simulation of the convection zone is also in good agreement with the results of the one-dimensional TYCHO model, including the velocity scale and background stratification estimated using mixing length theory. (3) The dynamics in the stably stratified layers in the simulation agree well with the analytic solutions to the non-radial wave equation, including the decomposition of the flow into specific, unambiguous modes (Meakin & Arnett 2006a). (4) The fluctuation amplitudes at the convective boundaries which are due to wave motions are found to be in good agreement with analytic

estimates for their scale.

Contrary to the assertion made by Almgren et al. (2006) that compressible codes should fail for $M < 10^{-2}$, we find a robust solution that agrees with an anelastic method for the same region simulated. Additionally, recent compressible simulations of He shell flash convection by Herwig et al. (2006) using the finite-volume Godunov code RAGE (Baltrusaitis et al. 1996) find a flow with $M \sim 10^{-3}$, with apparently robust results, including well behaved g-modes. Almgren et al. (2006) present an example simulation illustrating the failure of PPM to track temperature for a simple flow with Mach number $M \sim 0.05$. This calculation, however, uses a compressible PPM code (FLASH) with two major differences from ours (PROMPI): they used the hydrodynamic procedure described in Zingale, et al. (2002) to remove the hydrostatic pressure from the Riemann solver, and their stellar model was much more degenerate than ours (the equation of state tends to become independent of temperature under their conditions, and care must be taken with cancellation of terms).

This work was supported in part by the ASCII FLASH center at the University of Chicago. One of us (DA) wishes to thank the Aspen Center for Physics for their hospitality.

REFERENCES

- Almgren, A. S., Bell, J. B., Rendleman, C. A., & Zingale, M. 2006, *ApJ*, 637, 922
 Arnett, D., 1994, *ApJ*, 427, 932
 Asida, S.M., & Arnett, D. 2000 *ApJ*, 545, 435
 Baltrusaitis, R. M., Gittings, M. L., Weaver, R. P., Benjamin, R. F., & Budzinski, J. M. 1996, *Physics of Fluids*, 8, 2471
 Bazàn, G., & Arnett, D. 1998, *ApJ*, 494, 316
 Carruthers, D. J., & Hunt, J. C. R. 1986, *Journal of Fluid Mechanics*, 165, 475
 Colella, P., & Woodward, P., 1984, *J. Chem. Phys.*, 54, 174
 Fryxell, B., Müller, E., & Arnett, D., 1989, *ApJ*, 367, 619
 Glatzmaier, G. A., 1984, *J. Chem. Phys.*, 55, 461

- Glatzmaier, G. A., & Roberts, P. H., 1995, *Nature*, 377, 203
- Gough, D. O. 1969, *Journal of Atmospheric Sciences*, 26, 448
- Herwig, F., Freytag, B., Hueckstaedt, R. M., & Timmes, F. X. 2006, *ApJ*, 642, 1057
- Hossain, M., & Mullan, D. J. 1993, *ApJ*, 416, 733
- Kippenhahn, R. & Weigert, A. 1990, *Stellar Structure and Evolution*, Springer-Verlag
- Kuhlen, M., Woosley, S. E., & Glatzmaier, G., *3D Stellar Evolution*, ed., Turcotte, S., Keller, S. C., & Cavallo, R. M., A.S.P. Conf. Series 293
- Lighthill, J. 1978, *Waves in Fluids* (Cambridge: Cambridge University Press)
- Lin, D. J., Bayliss, A., & Taam, R. E. 2006, *ArXiv Astrophysics e-prints*, arXiv:astro-ph/0606207
- Livne, E., 1993, *ApJ*, 406, 17
- Meakin, C., & Arnett, D., *ApJ*, 637, 53
- Meakin, C., & Arnett, D., in preparation.
- Press, W. H. 1981, *ApJ*, 245, 286
- Rauscher, T., & Thielemann, K.-F., 2000, *Atomic Data Nuclear Data Tables*, 75, 1
- Rogers, T. M., & Glatzmaier, G. A., *ApJ*, 620, 432
- Schneider, T., Botta, N., Geratz, K. J., & Klein, R. 1999, *Journal of Computational Physics*, 155, 248
- Timmes, F. X. & Swesty, F. D. 2000, *ApJS*, 126, 501
- Unno, W., Osaki, Y., Ando, H., Saio, H., & Shibahashi, H. 1989, *Nonradial oscillations of stars*, Tokyo: University of Tokyo Press, 1989, 2nd ed.,
- Weaver, T. A., Zimmerman, G. B., & Woosley, S. E. 1978, *ApJ*, 225, 1021
- Young, P. A. & Arnett, D. 2005, *ApJ*, 618, 908
- Young, P. A., Meakin, C., Arnett, D., Fryer, C., 2006, *ApJ*, 629, L101
- Young, P. A., Fryer, C., Hungerford, A., Arnett, D., Rockefeller, G., Timmes, F. X., Voit, B., Meakin, C., Eriksen, K. A., 2006, *ApJ*, 640, 891
- Zingale, M., et al., 2002, *ApJS*, 143, 539

TABLE 1
COMPARISON OF OXYGEN BURNING MODELS

Variable	Units	2D-PPM	3D-PPM	3D-Anelastic ¹
M_* ^a	(M_\odot)	23	23	25
M_{in}, M_{out} ^b	(M_\odot)	1.0(1.5), 2.7(2.4)	1.0(1.5), 2.7(2.4)	1.2, 2.3
r_{in}, r_{out} ^b	(10^9 cm)	0.3(0.44), 1.0(0.85)	0.3(0.44), 1.0(0.85)	0.45, 0.84
L_{net} ^c	(erg/s)	3.2×10^{46}	3.5×10^{46}	1.5×10^{45}
$\Delta\theta, \Delta\phi$	(deg.)	90	30, 30	360, 180
Zones/Modes	($n_r \times n_\phi \times n_\theta$)	$400 \times 320 \times 1$	$400 \times 100 \times 100$	$145 \times 63(l) \times 31(m)$
v_{max}	(10^7 cm/s)	7.2	3.8	1.8
$\langle v_{conv} \rangle$	(10^7 cm/s)	2.0	0.8	0.49
M_{peak}	-	0.163	0.09	~ 0.04
M_{rms}	-	0.03	0.01	~ 0.01
t_{conv}	(s)	40	103	159
t_{max}	(s)	2400	800	6500
$\max\{ \rho'_c / \langle \rho \rangle \}$ ^d	10^{-2}	$1.0(6.0)^e$	0.5	0.2
$\max\{ T'_c / \langle T \rangle \}$	10^{-2}	0.25	0.05	0.06
$\max\{ \rho'_b / \langle \rho \rangle \}$	10^{-2}	12.0	11.0	-
$\max\{ T'_b / \langle T \rangle \}$	10^{-2}	2.7	1.0	-

¹The values quoted for the 3D anelastic model are from Kuhlen, Woosley, & Glatzmaier (2003).

^aZero age main sequence mass.

^bValues in parentheses indicate the extents of the convection zone for the compressible models and the other values indicate the extents of the entire computation domain including the stable layers.

^cThe net luminosity for the compressible models, $L_{net} = \int (\epsilon_{nuc} + \epsilon_{\nu\bar{\nu}}) dM$, is estimated at $t \sim 400$ s and is slowly decreasing with time due to an overall background expansion occurring within the burning region.

^dThe c and b subscripts indicate thermodynamic fluctuation amplitudes that are estimated in the convection zone and in the region of the convective boundary, respectively.

^eThe value in parentheses is the maximum density fluctuation estimated over two convective turnovers while the other value represents the time averaged maximum fluctuation. The significantly larger fluctuations seen in the 2D model compared with those in the 3D model occur near the center of large vortices which persist for several convective turnover times in the 2D model but are absent in the 3D convective flow.